PAPER

Check for updates

Physico-chemical properties of selenium–tellurium alloys across the scales

Luke D. Geoffrion [ID] and Grégory Guisbiers [ID] *

Selenium and tellurium are both energy critical elements as defined by the American Physical Society and the Materials Research Society. When mixed together, both elements form an alloy. The size- and shape-dependent thermal and optical properties of this alloy are investigated in this manuscript by using nano-thermodynamics and machine learning techniques. This alloy is found to have particularly interesting properties for solar cell applications.

1. Introduction

Selenium (Se) and tellurium (Te) are chalcogenide elements (*i.e.* they belong to the oxygen column in the periodic table) that have been classified as energy critical elements by the American Physical Society (APS) and the Materials Research Society (MRS).[1,2] Se and Te are not abundant in the Earth's crust and they have crustal abundances of 0.130 ppm (ref. 3) and 0.001 ppm,[4] respectively. Due to their scarcity, they cannot be mined directly and are recovered as by-products of copper refining.[5] Due to the non-homogeneous geographic repartition of copper ores around the world, only a small number of countries have access to most of the world reserves of Se and Te (Fig. 1a and b) maintaining their prices above ~$25 per kilogram (Fig. 1c). The worldwide consumption of Se and Te is illustrated in Fig. 1d and e. Specifically, Se is used essentially for metallurgy (30%), glass manufacturing (25%), agriculture (10%), chemicals (10%), electronics (10%) and some other minor uses (5%), while Te is used for solar cells (40%), thermoelectrics (30%), metallurgy (15%), rubber manufacturing (5%) and some other minor uses (10%). Currently, there is an increasing demand for Se to be used in copper–indium–gallium–diselenide (CIGS) solar cells[6] and for Te to be used in cadmium telluride (CdTe) solar cells,[7] making the domestic availability of these chalcogenide elements at risk. Se is now even added to CdTe to boost solar cell efficiency up to 22%.[8] Se and Te are used in solar cells due to their energy bandgaps (1.79 and 0.33 eV, respectively),[9] which allow them to absorb light in the visible and near infrared regions, respectively. A broadband solar absorber made exclusively of Te nanoparticles, with a size distribution ranging from 10 nm to 300 nm, has achieved more than 85% absorption of the solar radiation.[10] Furthermore, Se is also used in lithium–selenium batteries for its electrical and electrochemical properties.[11–13] Due to their low glass transition

and crystallization temperatures, Se and Te are also widely used as phase change memory materials.[14] Besides their use in electronics and optoelectronics, Se and Te are both used in medicine as antibacterial,[15–17] antifungal,[18] and anticancer drugs.[19] For this type of application, the chalcogenide elements are synthesized as nanoparticles suspended in a solvent, consequently, forming a colloidal solution.[18,20]

Most of the scientific research regarding Se and Te has been focusing on each chemical element separately; however the two chemical elements can easily form an alloy, $Se_{1-x}Te_x$, which allows a fine tuning of the physico-chemical properties through the control of its chemical composition. Relatively few papers have been published on this alloy and besides the chemical composition used to tune the physico-chemical properties of the $Se_{1-x}Te_x$ alloy, other variables such as size and shape were also studied. Indeed, $Se_{1-x}Te_x$ thin films,[21–24] nanorods[25] and nanowires[26] were successfully prepared and characterized.

From a theoretical point of view, several techniques have been developed to predict the physico-chemical properties of alloys at the nanoscale. The Monte Carlo method was the first one to appear in the '40s,[27] followed by molecular dynamics in the '50s,[28] nano-thermodynamics in the '60s,[29] and Density Functional Theory (DFT) in the '70s.[30] Machine learning flourished in physical chemistry during the 2010's and grew as a separate field from artificial intelligence.[31,32] Among those techniques, nano-thermodynamics is certainly the lesser known.[33–38] It is only in 2001 that nano-thermodynamics was brought to broad daylight, due to an invited paper written by the pioneer of nano-thermodynamics "Terrence Hill" who published his ideas on thermodynamics of small systems in the first volume of Nano Letters.[39,40] The ideas used in nano-thermodynamics allow the prediction of various material properties at the nanoscale such as phase diagrams.[33,36,41]

In this manuscript, nano-thermodynamics and machine learning techniques are used to predict the binary phase diagram, the surface segregation, Debye and Einstein temperature, glass and crystallization transition temperatures, and

Department of Physics & Astronomy, University of Arkansas at Little Rock, 2801 South University Avenue, Little Rock, AR 72204, USA. E-mail: gxguisbiers@ualr.edu
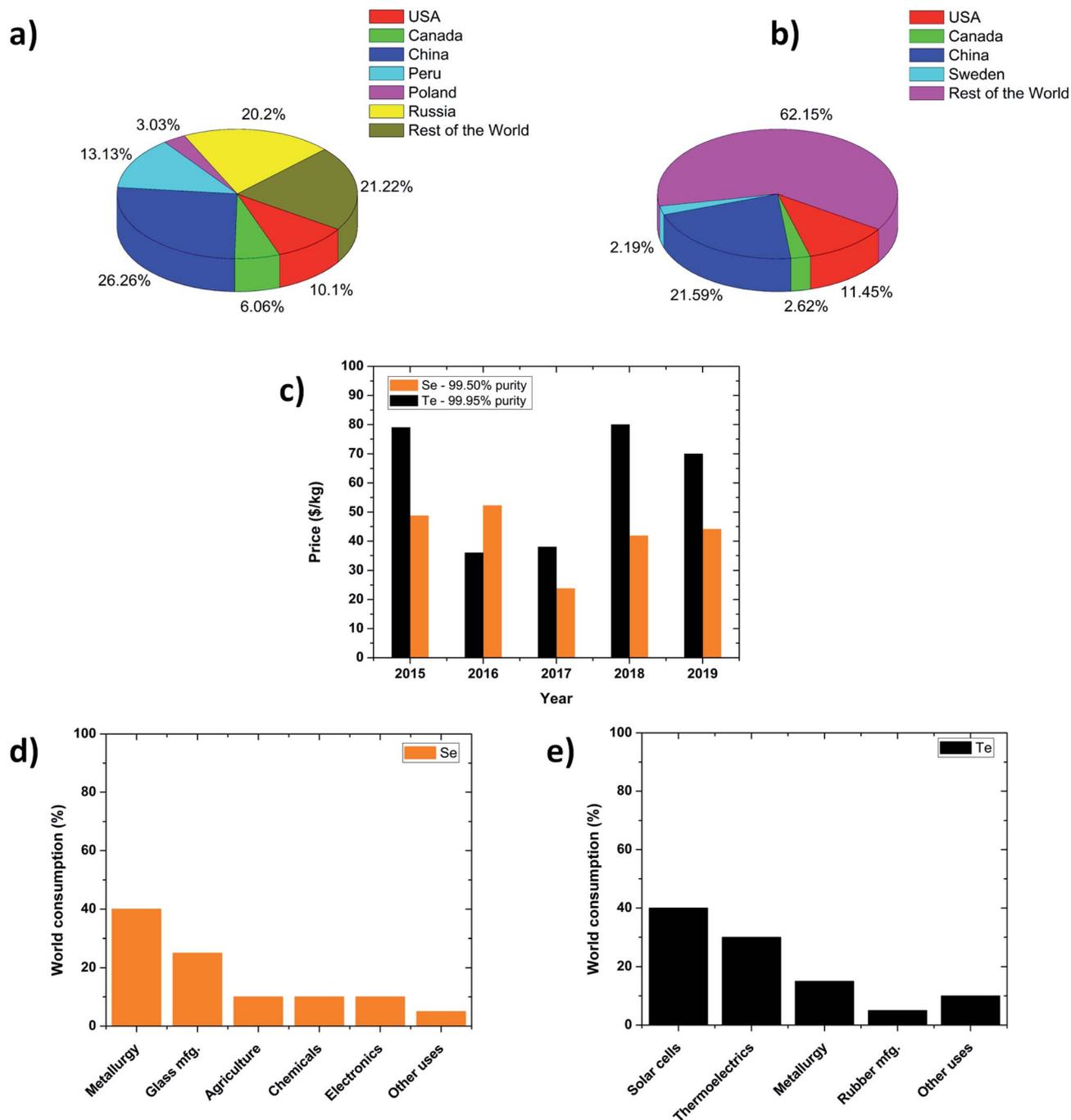
Fig. 1   World reserves of (a) selenium and (b) tellurium. The 2020 data come from the U.S. Geological Survey (USGS).[80] (c) Price per kilogram of material as a function of time. The time period covers the last 5 years. World consumption of (d) selenium and (e) tellurium. All data come from the USGS.[80]

finally the optical properties including the bandgap, refractive index, dielectric constant, and exciton Bohr radius of $Se_{1-x}Te_x$. All the thermal properties are discussed as a function of chemical composition while the optical properties are additionally discussed as functions of crystallinity. After presenting the theory, each result is discussed individually at the bulk- and nano-scales with respect to the available experimental data. Finally, the most important material properties of $Se_{1-x}Te_x$ are summarized in the conclusion.

2.   Binary phase diagram

In order to understand the formation of $Se_{1-x}Te_x$ at the bulk scale, let's analyze the Hume-Rothery rules which are a set of basic rules that describe the conditions under which two chemical elements can form a solid solution.[42] The rules state that an alloy forms if the chemical elements involved in the binary compound have similar crystal structures, similar electronegativity, similar valence, and a difference between their

respective atomic radii less than 15%. According to Table 1, Se and Te have the same hexagonal crystal structure (hcp), the same valence (+6), similar electro negativities (~6% difference), and a difference between their atomic radii of 14.6%, just below the 15% threshold, therefore satisfying all the conditions. Since all of these conditions are met, the bulk phase diagram of $Se_{1-x}Te_x$ should display complete miscibility across the entire temperature–composition space.[43,44]

To determine quantitatively the phase diagram of a binary alloy ($A_{1-x}B_x$), the composition (%) of the alloy in the liquid and solid states (x_l, x_s, respectively) has to be determined at each temperature T (K), while the total Gibbs free energy of the alloy, G_{total} (J mol^{-1}), must be minimized. The total Gibbs free energy is given by the following equation:[36]

$$G_{total} = x_l G_l(x_B,T) + x_s G_s(x_B,T) \quad (1a)$$

where x_B (%) is the molar percent of element B in the alloy, T (K) is the temperature. G_l (J mol^{-1}) and G_s (J mol^{-1}) are the Gibbs free energy of the liquid and solid phases, respectively, which are described by the following equations:[36]

$$G_l(x_B,T) = RT[x_B \ln x_B + (1 - x_B)\ln(1 - x_B)] + \Omega_l x_B(1 - x_B) \quad (1b)$$

$$G_s(x_B,T) = RT[x_B \ln x_B + (1 - x_B)] + \Omega_s x_B(1 - x_B) + (1 - x_B)\Delta H_m^A(T/T_m^A - 1) + x_B \Delta H_m^B(T/T_m^B - 1) \quad (1c)$$

where R (8.314 J mol^{-1} K^{-1}) is the ideal gas constant, ΔH_m^A (J mol^{-1}) and ΔH_m^B (J mol^{-1}) are the size-dependent melting enthalpies of elements A and B respectively, T_m^A (K) and T_m^B (K) are the size dependent-melting points of elements A and B respectively, and Ω_l (J mol^{-1}) and Ω_s (J mol^{-1}) are the size-dependent enthalpies of mixing for the liquid and solid state respectively.

For each temperature T, between the melting points of the two chemical elements (A $\equiv$ Se and B $\equiv$ Te) constituting the alloy, the compositions that minimize the total Gibbs free energy are determined. Therefore, at equilibrium, when the solid and liquid phases coexist ($G_l = G_s$), the solutions of eqn (1) form the *solidus* and *liquidus* curves in the binary phase diagram.

By using the bulk material properties of Se and Te listed in Table 1, the *solidus–liquidus* curves of $Se_{1-x}Te_x$ are displayed in Fig. 2a. The excellent agreement between the calculated bulk phase diagram and the experimental data points, Fig. 2a, proved that the phase diagram is described well by the sub-regular solution model (eqn (1)).

To determine the binary phase diagram of $Se_{1-x}Te_x$ at the nanoscale, all the size-dependent material properties involved in eqn (1) have to be calculated. In order to evaluate those values, the following scaling law is used:[36,45]

$$\frac{T_m(D)}{T_{m,\infty}} = \frac{\Delta H_m(D)}{\Delta H_{m,\infty}} = \frac{\Omega_s(D)}{\Omega_{s,\infty}} = \frac{\Omega_l(D)}{\Omega_{l,\infty}} = 1 - \frac{\alpha_{shape}}{D} \quad (2)$$

where $\alpha_{shape} = \dfrac{AD(\gamma_s - \gamma_l)}{V\Delta H_{m,\infty}}$ represents the size/shape effect on the material, D is the characteristic size of the nanostructure, A/V is the surface to volume ratio (Table 2), and γ_s and γ_l are the solid and liquid surface energy, respectively. $T_{m,\infty}$, $\Delta H_{m,\infty}$, $\Omega_{s,\infty}$ and $\Omega_{l,\infty}$ are the bulk melting temperature, bulk melting enthalpy, and bulk enthalpy of mixing for the solid and liquid phase, respectively (Table 1). The α_{shape} parameters for the sphere ($A/V = 6/D$), infinitely long wire ($A/V = 4/D$), and infinitely long and wide film ($A/V = 2/D$) morphologies are given in Table 2. The characteristic length, D, for the sphere, infinitely long wire, and infinitely long and wide film are the diameter, diameter, and the thickness, respectively. As expected, the α_{shape} parameter increases with increasing value of the surface-to-volume ratio, which results in $\alpha_{sphere} > \alpha_{wire} > \alpha_{film}$.

At the nanoscale, the lens-shape of the *solidus–liquidus* curves is preserved, but shifted to lower temperatures when compared to the bulk phase diagram; see Fig. 2b–d. For all the morphologies considered (sphere, wire, and film), a broadening effect is noted; *i.e.* as the size is decreased, the temperature difference between the *solidus* and *liquidus* curves increases. This effect is related to the mixing enthalpy of the solid phase. Indeed, as the size decreases the mixing enthalpy of the solid phase increases, because the mixing enthalpy is negative all across the composition range; see Fig. 3. This indicates that the broadening effect should be observed in all binary alloys that have a negative mixing enthalpy at the bulk scale.

It is important to note that nanoparticles undergo mainly two types of melting: homogeneous melting and heterogeneous melting.[46] With the homogeneous melting, the solid particle is always at equilibrium with the melted one. With the heterogeneous melting, a liquid layer nucleates at the surface of the

Table 1 Bulk material properties of selenium (Se) and tellurium (Te)

Material property	Se	Te	Ref.
Crystalline structure	Hexagonal	Hexagonal	9
Atomic radius (pm)	117	137	9
Valence	+6	+6	9
Electron affinity (eV)	2.02	1.97	9
1st ionization energy (eV)	9.7524	9.0096	9
Mulliken electronegativity^a (eV)	5.88	5.50	a
a (pm)	237	283	9
$T_{g,\infty}$ (K)	350	—	43
$T_{m,\infty}$ (K)	494	723	9
$\Delta H_{m,\infty}$ (kJ mol^{-1})	6.694	17.376	9
ΔH_{vap} (kJ mol^{-1})	90	104.5	9
γ_l (J m^{-2})	0.106	0.186	9
γ_s (J m^{-2})	0.291	0.355	77 and 78
Ω_l (J mol^{-1})	$x_{Se}x_{Te}[(-8271.5 + 8.78843T) + 467.8(x_{Se} - x_{Te})]$		43
Ω_s (J mol^{-1})	$x_{Se}x_{Te}(-222.6 - 1.2815T)$		43
$Q_{seg,\infty}$ (kJ mol^{-1})	−16.8		This work
η	0.147	0.125	This work
$\theta_{D,\infty}$ (K)	150	141	79
$\theta_{E,\infty}$ (K)	134	83^b	58 and 59
E_g (eV)	1.79	0.33	9
μ (m_e)	0.08	0.01775	This work

^{a} Calculated by taking the average of the electron affinity and the 1st ionization energy. ^{b} Using value for a film with grain size greater than 1000 nm from ref. 58.
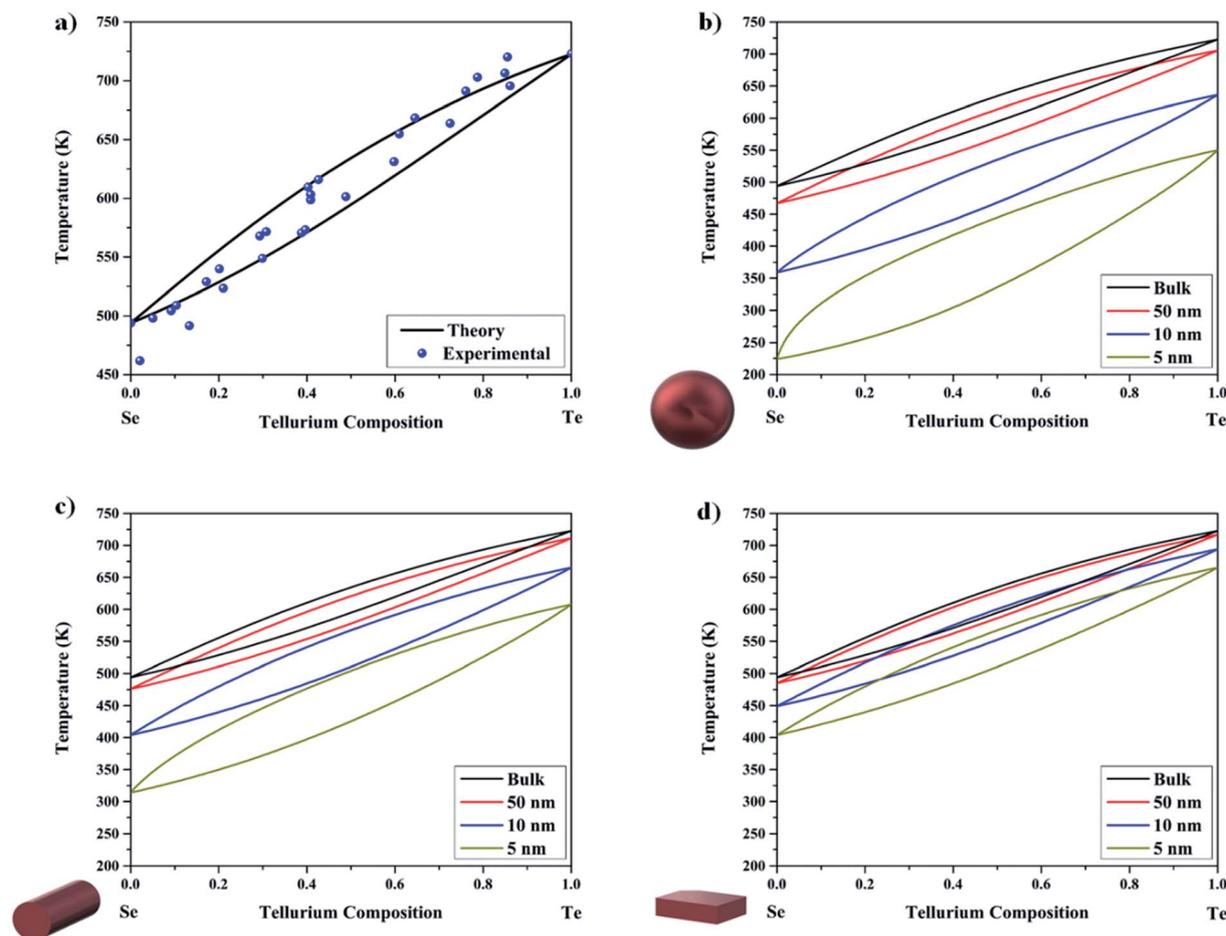
Fig. 2 (a) Binary phase diagram of the bulk $Se_{1-x}Te_x$ alloy displaying the *solidus–liquidus* curves (eqn (1)). Experimental data points are taken from ref. 81. Binary phase diagram for the $Se_{1-x}Te_x$ alloy displaying the *solidus–liquidus* curves (eqn (1) and (2)) at the nanoscale (50, 10 and 5 nm) for the (b) sphere, (c) wire, and (d) film morphologies.

Table 2 Parameters quantifying the size effect on selenium (Se), tellurium (Te) and $Se_{1-x}Te_x$ for the sphere, wire, and film morphologies

Shape	α_{shape}^{Se} (nm)	α_{shape}^{Te} (nm)	$\alpha_{shape}^{Se_{1-x}Te_x}(x)$ (nm)
Sphere	2.733	1.193	$2.733 - 1.540x$
Wire	1.822	0.796	$1.822 - 1.026x$
Film	0.911	0.398	$0.911 - 0.513x$

particle and grows with temperature; this is also called "surface melting". Both types of melting predict a linear relationship between the melting temperature and the reciprocal size of the particle. Consequently, they can be described by eqn (2), but the value of α_{shape} will be different in each case.[46] Surface melting has already been observed in metallic gold nanoparticles by *in situ* transmission electron microscopy.[47] The shape transformation of gold nanoparticles was caused by surface melting.[48] However, here we are studying two semiconductors Se and Te which have a much smaller Hamaker constant compared to gold, consequently hindering surface melting.[49] Therefore, no surface melting was considered in this manuscript.
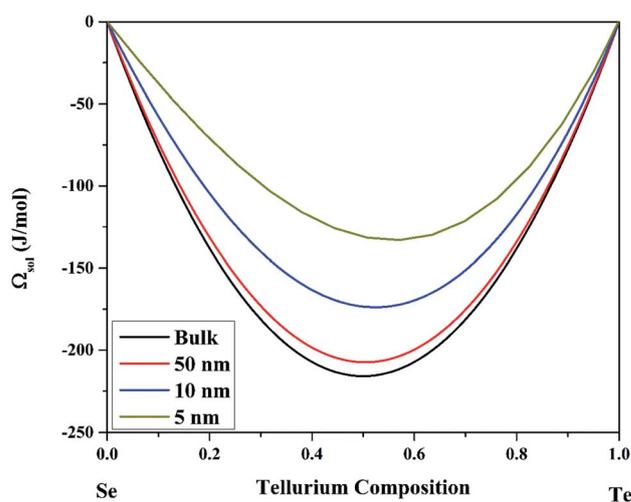

Fig. 3 Size-dependent enthalpy of mixing at 500 K for the solid solution of $Se_{1-x}Te_x$ alloy considering the spherical morphology.

3. Surface segregation

Shrinking the size of an alloy to the nanoscale is often accompanied by some surface segregation. Indeed, there is always a natural tendency between the two chemical elements that one of the two prefers to be at the surface. In the seventies, Williams and Nason[50] predicted the surface segregation of binary compounds by describing the enrichment of the outermost layer of the material only. According to their model, the surface composition of the binary alloy is given by:[50]

$$x_{\text{solidus}}^{\text{surface}} = \frac{\dfrac{x_{\text{solidus}}^{\text{core}}}{1 - x_{\text{solidus}}^{\text{core}}}\, e^{-\Delta H_{\text{sub}} z_{1v}/z_1 RT}}{1 + \dfrac{x_{\text{solidus}}^{\text{core}}}{1 - x_{\text{solidus}}^{\text{core}}}\, e^{-\Delta H_{\text{sub}} z_{1v}/z_1 RT}} \tag{3a}$$

$$x_{\text{liquidus}}^{\text{surface}} = \frac{\dfrac{x_{\text{liquidus}}^{\text{core}}}{1 - x_{\text{liquidus}}^{\text{core}}}\, e^{-\Delta H_{\text{vap}} z_{1v}/z_1 RT}}{1 + \dfrac{x_{\text{liquidus}}^{\text{core}}}{1 - x_{\text{liquidus}}^{\text{core}}}\, e^{-\Delta H_{\text{vap}} z_{1v}/z_1 RT}} \tag{3b}$$

where $x_{\text{solidus}}^{\text{core}}$ (%) and $x_{\text{liquidus}}^{\text{core}}$ (%) are the size-dependent *solidus* and *liquidus* composition given by minimizing the Gibbs' free energy when no surface segregation effect is considered. ΔH_{vap} (J mol^{-1}) and ΔH_{sub} (J mol^{-1}) are the absolute difference between the two pure elements for the vaporization enthalpy and sublimation enthalpy, respectively. z_{1v}/z_1 is the ratio between the number of atoms in the vertical direction and the coordination number; those numbers are equal to 2 and 3, respectively, for the hexagonal structure of Se and Te.

Tománek *et al.*[51] described surface segregation in terms of a surface segregation energy, representing the work involved in exchanging a surface atom with a core atom. This concept is described for a bulk material (eqn (4a)) and a nano material (eqn (4b)) by the following equations, respectively:[51]

$$\frac{x_{\text{surface}}}{1 - x_{\text{surface}}} = \frac{x_{\text{core}}}{1 - x_{\text{core}}}\, e^{Q_{\text{seg},\infty}/RT} \tag{4a}$$

$$\frac{x_{\text{surface}}}{1 - x_{\text{surface}}} = \frac{x_{\text{core}}}{1 - x_{\text{core}}}\, e^{Q_{\text{seg}}/RT} \tag{4b}$$

where x_{surface} (%) and x_{core} (%) are the composition of the surface and the core of the material, respectively, R (J mol^{-1} K^{-1}) is the ideal gas constant, and T (K) is the temperature. $Q_{\text{seg},\infty}$ (J mol^{-1}) and Q_{seg} (J mol^{-1}) are the surface segregation energy at the bulk and nanoscale, respectively. As surface segregation is also size-dependent, Guisbiers *et al.*[52] described the size effect on the surface segregation energy as:

$$\frac{Q_{\text{seg}}(D)}{Q_{\text{seg},\infty}} = 1 - \frac{\alpha_{\text{shape}}}{D} \tag{4c}$$

By using the *solidus* data from Fig. 2b–d as the core composition within eqn (3a), the surface segregation in nanoparticles, wires, and films can be predicted (Fig. 4a–c). Indeed, Fig. 4a–c show the plot of the surface composition of the nanostructure, x_{surface} (%) *versus* its core composition, x_{core} (%). The *x*-axis of Fig. 4a–c can be understood as when the core composition is zero the structure is only made of Se, while when the core composition equals one, the structure is only made of Te. When the core composition varies between zero and one, the surface composition does not evolve linearly with the core composition anymore. As seen in Fig. 4a–c, Se segregates to the surface.

The bulk surface segregation energy of Se$_{1-x}$Te$_x$ has been determined as −16.8 kJ mol^{-1}, by equaling eqn (4a) to eqn (3a). The value reported here is comparable to the surface segregation energy reported for Bi$_{1-x}$Sb$_x$,[53] −15.7 kJ mol^{-1}, and for Ni$_{1-x}$Pd$_x$,[51] −16.8 kJ mol^{-1}. In those alloys, it was demonstrated that Bi and Pd were the chemical elements segregating preferentially to the surface of Bi$_{1-x}$Sb$_x$, and Ni$_{1-x}$Pd$_x$, respectively. The surface segregation is enhanced as the surface-to-volume ratio increased.

According to Guisbiers *et al.*,[54] in the case of total miscibility the material with the highest melting point should segregate to the surface, but this is not the case in Se$_{1-x}$Te$_x$. When developing their rules, they only considered face centered cubic (f.c.c.) alloy systems; therefore, due to the hexagonal crystal structure of Se$_{1-x}$Te$_x$, it does not follow the rules described in ref. 54. This suggests that the rules need to be revised when considering hexagonal crystal systems.

In Fig. 4d, the Surface Segregation Index (SSI) of Se$_{1-x}$Te$_x$ is calculated *versus* the size of the structure. The SSI was defined in ref. 53, as the surface area between the no segregation line and the segregated line in a plot displaying the surface composition *versus* core composition (Fig. 4a–c). When SSI is negative, Se is found to be preferentially at the surface while when SSI is positive, Te is found preferentially at the surface. This index helps to quantify the intensity of the surface segregation. The SSI becomes more negative as the size of the Se$_{1-x}$Te$_x$ structure decreases. In absolute value, the sequence SSI$_{\text{sphere}}$ > SSI$_{\text{wire}}$ > SSI$_{\text{film}}$ is observed because α_{sphere} > α_{wire} > α_{film}.

4. Debye and Einstein temperatures

The bulk Debye temperature, $\theta_{\text{D},\infty}$ (K) is the temperature of a material's highest normal mode of vibration, *i.e.*, the highest temperature that can be achieved due to a single phonon.[55]

$$\theta_{\text{D},\infty} = \frac{\hbar \omega_{\text{D},\infty}}{k_{\text{B}}} \tag{5}$$

where $\hbar$ is the reduced Planck's constant (J Hz^{-1}), k_{B} is the Boltzmann's constant (J K^{-1}) and ω_{D} (Hz) is the maximal phonon frequency of the bulk material. The Debye temperature indicates the approximate temperature limit below which quantum effects may be observed.

The Debye temperature is closely related to the melting temperature through Lindeman's melting criterion.[56,57] Indeed, according to Lindeman, solids liquefy when the amplitude of vibration exceeds a fraction of the interatomic spacing. The modern form of Lindeman's criterion is given by:[57]

$$\theta_{\text{D},\infty} = \frac{1}{\eta\alpha}\left(\frac{T_{\text{m},\infty}}{\xi A}\right)^{\frac{1}{2}} \tag{6}$$
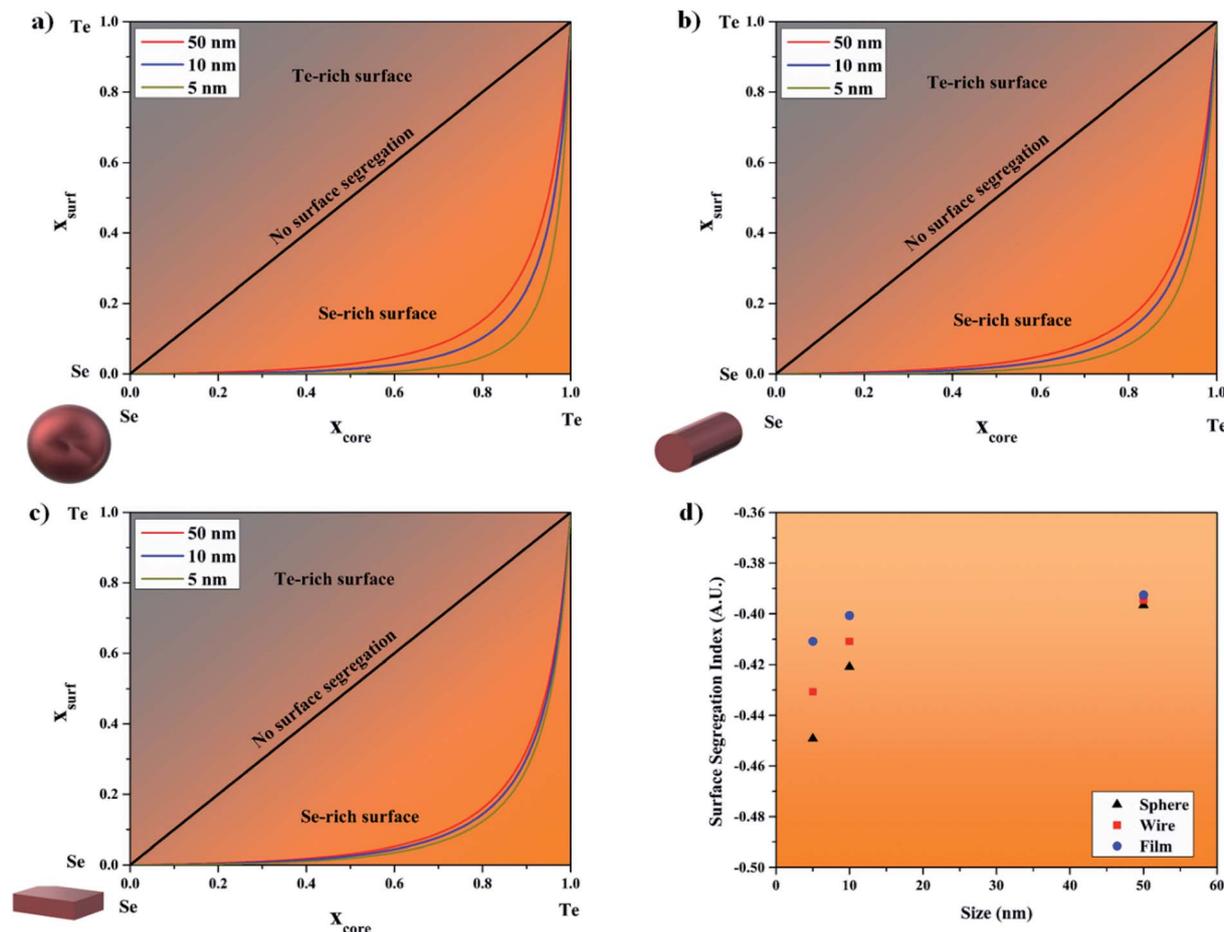
Fig. 4 Surface composition *versus* the core composition of the $Se_{1-x}Te_x$ alloy at the solidus temperature for the (a) sphere, (b) wire, and (c) film morphologies. (d) Surface segregation index as defined in ref. 53 *versus* the size of the nanostructure.

where η is the Lindeman coefficient, $\xi = 2.29 \times 10^{20}$ mol J^{-1} K^{-1} s^{-1}, A is the atomic mass, and α is the interatomic distance. From the data listed in Table 1, the Lindeman coefficients of Se and Te were determined at 0.147 and 0.125, respectively.

From Lindeman's criterion, the square of the Debye temperature is directly proportional to the melting temperature *i.e.* $\theta_{D,\infty}{}^2 \propto T_{m,\infty}$. Assuming that this relationship holds at the nanoscale, then we have:[45,55]

$$\frac{T_m}{T_{m,\infty}} = \left(\frac{\theta_D}{\theta_{D,\infty}}\right)^2 = 1 - \frac{\alpha_{shape}}{D} \quad (7)$$

The bulk Einstein temperature, $\theta_{E,\infty}$ (K) characterizes a bulk solid composed of single-frequency quantum harmonic oscillators. All the atoms are supposed to oscillate at the same frequency, called Einstein frequency, $\omega_{E,\infty}$ (Hz). Einstein's single frequency can be viewed as a kind of mean value of all the frequencies available in the Debye model. The bulk Einstein's temperature is defined as:[55]

$$\theta_{E,\infty} = \frac{\hbar\omega_{E,\infty}}{k_B} \quad (8)$$

As the Debye temperature and the Einstein temperature are proportional to each other, we consequently have:[55]

$$\frac{\theta_D}{\theta_{D,\infty}} = \frac{\theta_E}{\theta_{E,\infty}} = \sqrt{1 - \frac{\alpha_{shape}}{D}} \quad (9)$$

In Fig. 5, the Debye and Einstein temperatures of Se and Te nanostructures are plotted using eqn (10). The available experimental data are extracted from ref. 58 and [59] and used for comparison with the theoretical curves. As it can be seen in Fig. 5a, c and d, the theoretical curves are in good agreement with the available experimental data. In Fig. 5b, the theoretical curves are displayed without comparison to experimental data because the Debye temperature of Te nanostructures has not been reported yet at the nanoscale.

Furthermore, in an alloy like $Se_{1-x}Te_x$, the Debye temperature becomes composition dependent *i.e.* $Se_{1-x}Te_x$. Some evidence of composition dependence for the Debye Temperature of $Se_{1-x}Te_x$ is found in ref. 60 and [61]. In order to evaluate this temperature, the melting temperature in eqn (8) is substituted by the *solidus* temperature of the alloy. It is assumed that the material's molar volume varies with Vegard's law since
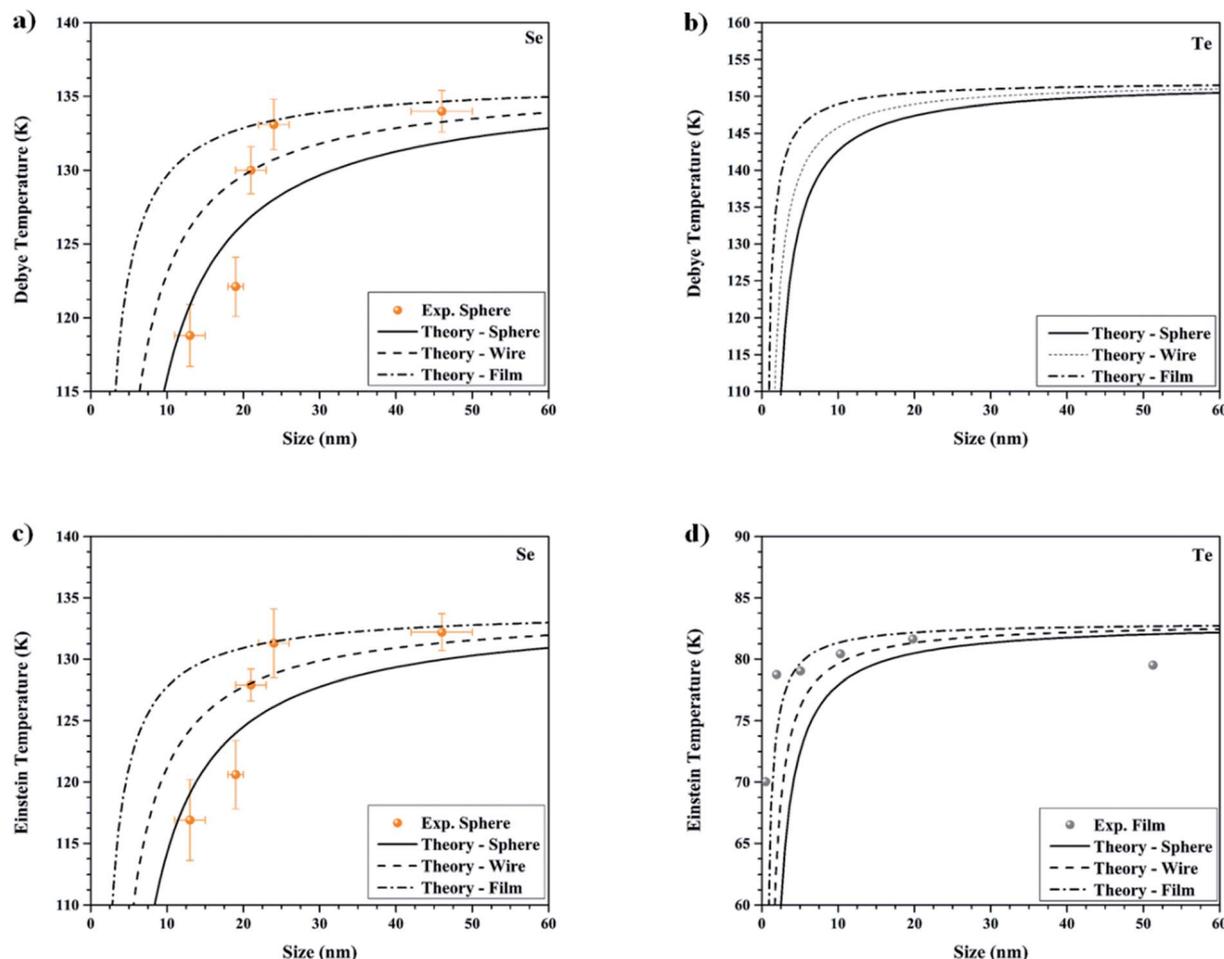
Fig. 5 Debye temperature *versus* the size of (a) Se nanostructures, (b) Te nanostructures. Einstein temperature *versus* the size of (c) Se nanostructures, (d) Te nanostructures. Experimental data for (a) and (c) are from ref. 59 for spherical nanoparticles, and (d) from ref. 58 for Te films.

the material's crystalline indices vary linearly throughout the entire composition range.[43]

Fig. 6 shows how the Debye temperature varies with increasing Te composition for the bulk, sphere, wire, and film morphologies in (a), (b), (c) and (d), respectively. Fig. 6a is obtained by using eqn (7). This shows that the Debye temperature varies non-linearly between pure Se and pure Te with that of Te being lower and that of Se being higher. When the size effect is applied, Fig. 6b–d, this changes significantly. At sizes around 10 nm for the spherical morphology, the Debye temperatures for pure Se and Te become almost equal, and below this size a tilting effect is noted, *i.e.*, the Debye temperature of Se is now lower and that of Te is higher.

5. Glass and crystallization temperatures

Depending on the kinetics of the cooling process, a solid may have two solidification paths, the crystallization path and the glass transition path. Indeed, the crystallization path displays the transition from a liquid into a crystalline solid which occurs

at the melting temperature, $T_{m,\infty}$; while the glass transition path displays the transition from a liquid into an amorphous solid which occurs at the glass temperature, $T_{g,\infty}$. Glass formation is a matter of bypassing crystallization by cooling down the liquid "fast enough" and "far enough". "Far enough" means that the cooling temperature must be well below the glass temperature of the material ($T < T_{g,\infty}$). "Fast enough" means that the cooling process to bring the liquid from a temperature $T_{m,\infty}$ to a temperature T lower than $T_{g,\infty}$ must be performed in a timeframe shorter than the crystallization time. Fig. 7a shows the process by which a material either becomes a glass or a crystal based on the volume of the material. As seen in Fig. 7b, there is some discrepancy in the data collected from ref. 24 and [43] in the measurement of the glass and crystallization temperatures of $Se_{1-x}Te_x$ alloys, which is due to the heating rate used in the experiments. Generally, when a slower heating rate is used the crystallization occurs at a lower temperature.

Prediction of glass temperature in an alloy is still an open question in materials science since no analytical or *ab initio* model can predict it accurately.[62] Therefore, machine learning techniques have been used to predict the transition
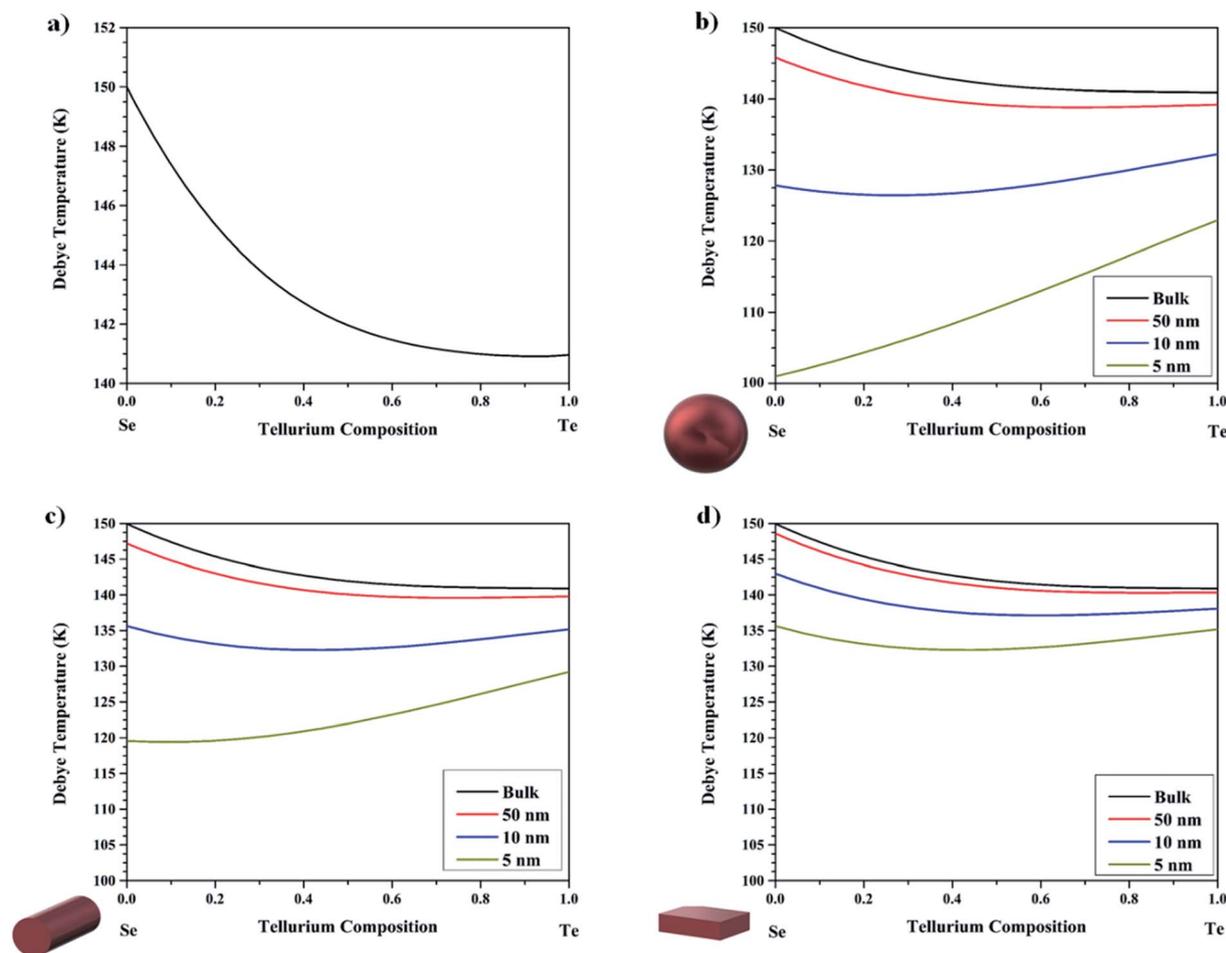
Fig. 6 Compositionally dependent Debye Temperature for the $Se_{1-x}Te_x$ alloy in the (a) bulk, and the (b) sphere, (c) wire, and (d) film morphologies.

temperature.[62] The points (composition, temperature) within the phase diagram underwent a binary classification allowing machine learning techniques to determine precisely the glass/crystallization boundary all across the phase diagram. Glass transition and crystallization were represented by 0 or 1, respectively. A logistic regression classifier was used to predict the region where the glass transition or crystallization would be likely to occur. Logistic regression was chosen as it is simple and has been applied widely in many fields.[31] It was implemented in python code utilizing the sklearn library.[63] The model validation was performed by choosing the model fitting parameters that resulted in the highest accuracy. In Fig. 7c, the output of the logistic regression model for the bulk $Se_{1-x}Te_x$ alloy is presented. From this figure, it is easy to see that the points above the line, in yellow, indicate the crystalline phase. Below this line, in cyan, the points represent the glass phase across the entire composition range. The model produced is simple and it is easily interpretable. Obviously, other models may produce a tighter fit on the data (K-Nearest Neighbors[64] or Artificial Neural Networks[65]), but these methods are difficult to interpret and generally overfit the data. This method gives a range of temperatures that experimentalists should investigate in order to detect a possible transition to the crystalline phase from the glassy one or from the liquid to the glass.

Like any other material property, the glass temperature is also size and shape-dependent.[55] It has been shown theoretically by Jiang et al.[55] and confirmed experimentally by Guisbiers et al.[66] that glass temperatures follow this type of scaling law:

$$\frac{T_g}{T_{g,\infty}} = 1 - \frac{\alpha_{shape}}{D} \tag{10}$$

where T_g (K) is the size/shape-dependent glass temperature and $T_{g,\infty}$ (K) is the bulk glass temperature. Following a reheating of the glassy material, crystallization may occur. Crystallization temperatures, $T_{c,\infty}$ (K), are always higher than the glass transition temperature of the material while also being lower than the melting temperature. Consequently, the crystallization temperature should follow the same trend as the melting temperature when looking at size and shape effects at the nanoscale, i.e.,

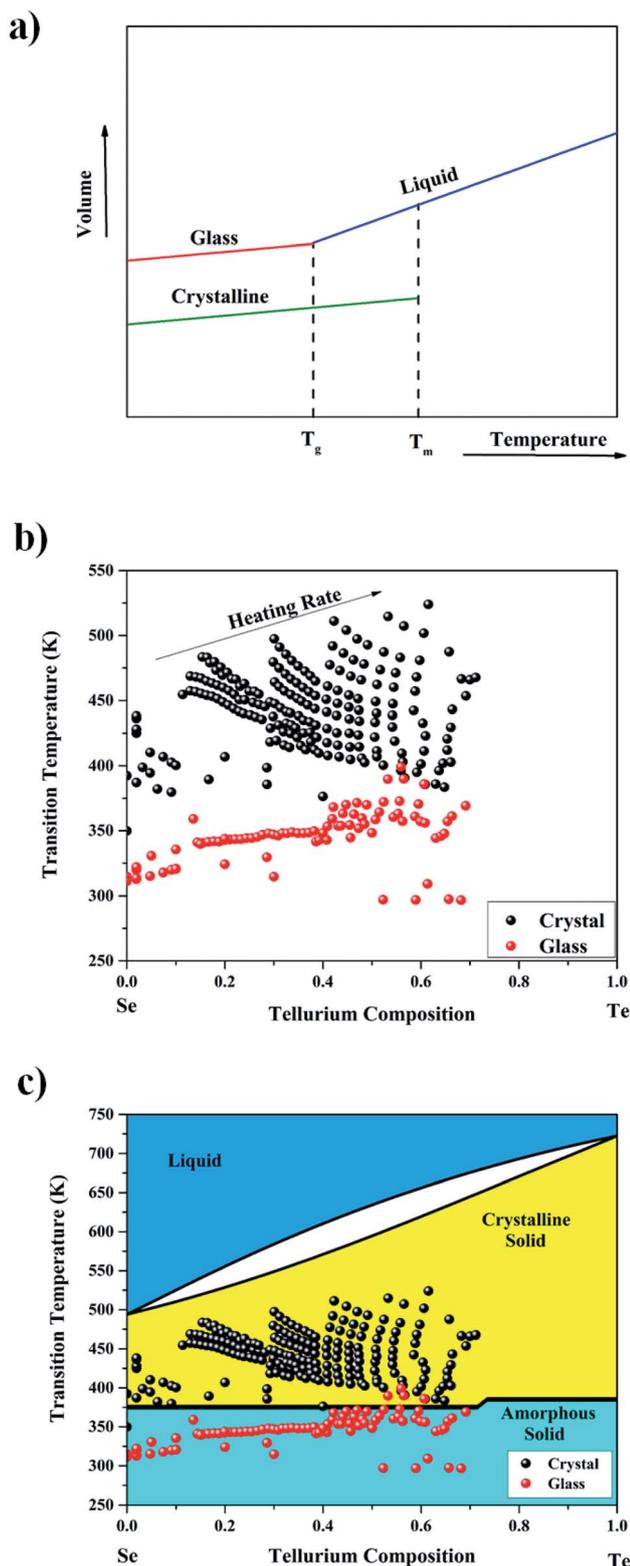$$\frac{T_c}{T_{c,\infty}} = 1 - \frac{\alpha_{shape}}{D} \tag{11}$$

Fig. 7 (a) Sketch representing the two possible scenarios for solidification, the crystallization path and the glass transition path. (b) Experimental data are from ref. 24, which were extracted by using the online tool WebPlotDigitizer,[82] and ref. 43. (c) Logistic regression classifier shows the boundary between the crystalline region and the amorphous region. Below this temperature, one should expect a glass transition; but above this temperature, one should expect a crystalline transition.

where T_c (K) is the size/shape dependent crystallization temperature and $T_{c,\infty}$ (K) is the bulk crystallization temperature.

Fig. 8 shows the same analysis as above but on the nanoscale counterpart. The data in this analysis were generated by applying the scaling laws (eqn (11) and (12)) to each data point. It is noted that as the size of the structure is decreased, the boundary starts tilting more towards the Se rich parts of the alloy, due to the much larger α_{shape} parameter of Se compared to Te.

6. Glass forming ability

Glass formation and glass stability are interesting properties of amorphous materials to study, and here we have described two criteria that we used to evaluate the $Se_{1-x}Te_x$ system. The ability of a material to form a glass during solidification has been termed the Glass-Forming Ability (GFA). One of the earliest criteria to determine the GFA was by using the reduced glass transition temperature defined as the ratio between the glass temperature and the melting temperature (the melting temperature is substituted by the *liquidus* temperature in the case of an alloy). Reduced glass transition is typically correlated with GFA or the minimum cooling rate to cause a glass to form. The results here are supported by the results for the cooling rates reported in ref. 24 where samples' minimum cooling rates evolved linearly with increase in Te composition. This implies that low reduced glass transition values correspond to very high cooling rates, leading to low GFA; see Fig. 9a. It is defined by the following equation:

$$T_{rg} = \frac{T_g}{T_m} \tag{12}$$

The reduced glass transition temperature, T_{rg}, is a unitless number varying between 0 and 1. It has been found to be a good indicator of GFA, *i.e.* the higher its value, the easier it is to form a glass. Turnbull suggested that at $T_{rg} \geq 2/3$, the crystallization is suppressed.[67] The reduced glass transition temperature considers only the Glass Forming Ability (GFA) but does not consider the Glass Stability (GS). Many other criteria exist in the literature to determine the GFA.[68,69] In order to consider GFA and GS at the same time, there is the Hruby's criterion:[14,70]

$$\chi = \frac{T_c - T_g}{T_m - T_g} \tag{13}$$

Hruby's criterion tells a similar story for the bulk material, Fig. 9a. This criterion is different from the reduced glass transition by being more sensitive to the crystallization temperature and not just the glass and *liquidus* temperatures. This is evident when investigating the samples where Te composition is above 0.4. Indeed, large spread in the data reveals sharp dips towards difficult glass formation, *i.e.*, below 0.1 in Hruby's criterion.

At the nanoscale, a similar story to that at the bulk scale is noticed. However, there is a burning question at the nanoscale: does having a nano-sized material help stabilize the glass
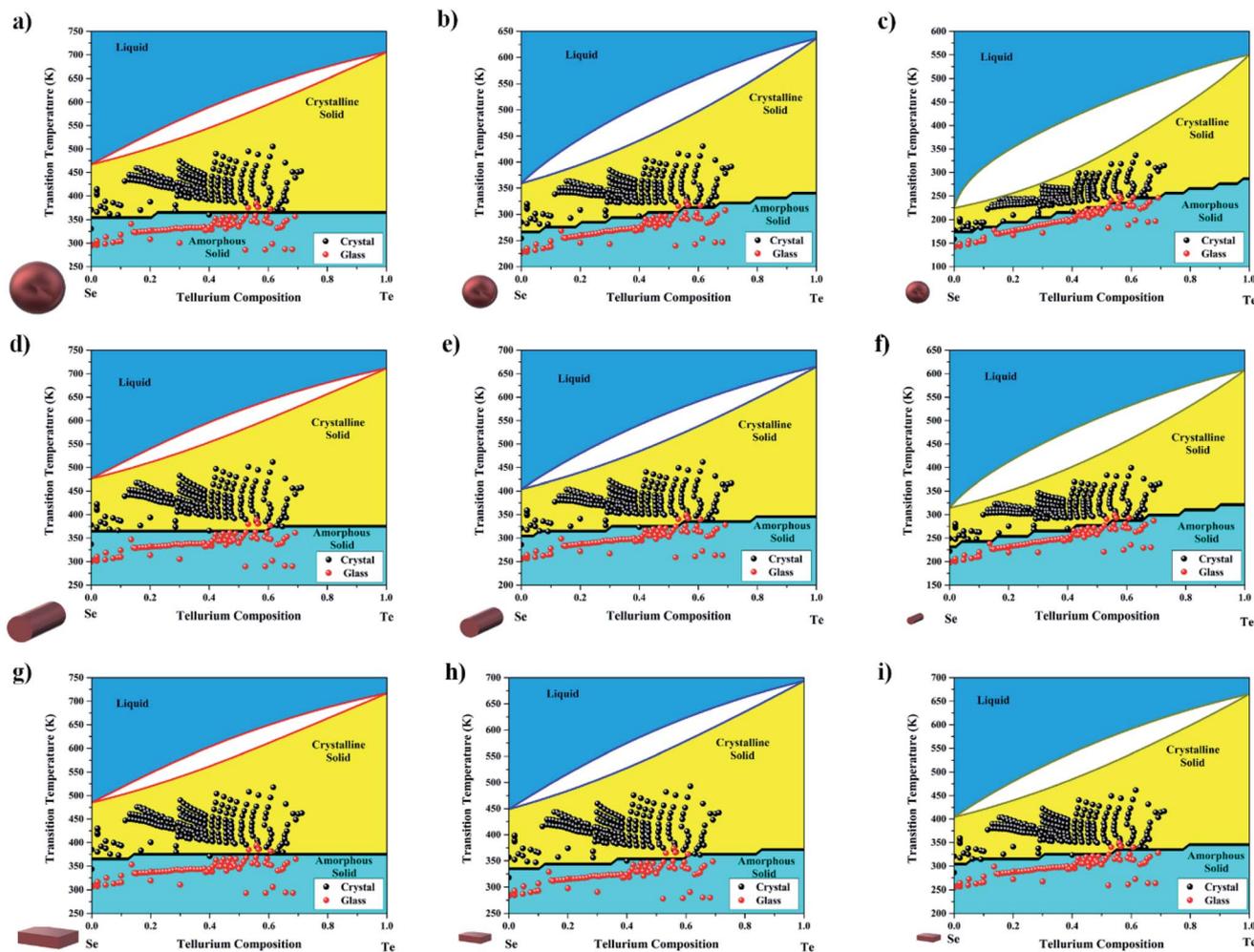
Fig. 8 (a, b, and c) Nano-sized glass (yellow) and crystalline (cyan) phases for spherical particles with sizes of 50 nm, 10 nm, and 5 nm, respectively. (d, e, and f) Nano-sized glass (yellow) and crystalline (cyan) phases for wire morphologies with sizes of 50 nm, 10 nm, and 5 nm, respectively. (g, h, and i) Nano-sized glass (yellow) and crystalline (cyan) phases for films with sizes of 50 nm, 10 nm, and 5 nm, respectively.

phase? The results plotted in Fig. 9b–c for the spherical nano-particles with sizes of 50 nm, 10 nm, and 5 nm do not support the claim that glass formation is more difficult at the nanoscale. Indeed, most of the data points stay above 0.1 threshold in Hruby's criterion, but the data underwent simply an overall shift downward. Physically this can be understood as when the size decreases, the number of particles in the system also decreases, which means that the number of degrees of freedom in the system is less in comparison to the bulk; and as such the number of possible movements that are available upon moving to a lower size are not there, *i.e.*, lower entropy in the nano-system.

7. Optical properties

At room temperature, $Se_{1-x}Te_x$ is a semiconductor all over its entire composition range. Therefore, it is interesting to look at the optoelectronic properties of this alloy as a function of its chemical composition, size, and shape. At the bulk scale, the optoelectronic properties of $Se_{1-x}Te_x$ are well understood;

however, very little is known regarding this material at the nanoscale.

At the bulk scale, the energy bandgap of $Se_{1-x}Te_x$ follows Vegard's law:[71]

$$E_g^{Se-Te}(x) = (1 - x)E_g^{Se} + xE_g^{Te} + bx(1 - x) \qquad (14)$$

where $E_g^{Se-Te}(x)$ is the energy bandgap of $Se_{1-x}Te_x$ at the composition x. E_g^{Se} (eV) and E_g^{Te} (eV) are the energy bandgap of Se and Te, respectively. b is the bowing parameter. The data gathered from ref. 21 suggest that b equals zero (*i.e.* $b_{amorphous} = 0$) when $Se_{1-x}Te_x$ is amorphous, and as such its energy bandgap exhibits a linear dependence with respect to the chemical composition, x (Fig. 10a). When $Se_{1-x}Te_x$ is crystalline, its energy bandgap does not follow a linear trend anymore but displays bowing characterized by the following bowing factor, $b_{crystalline} = 1.102$.[72] When crystalline, Se and Te have slightly different energy bandgap values as seen in ref. 72, 1.73 and 0.35 eV, respectively, due to the change in their lattice param-eter. As a note, glassy or amorphous $Se_{1-x}Te_x$ has not been
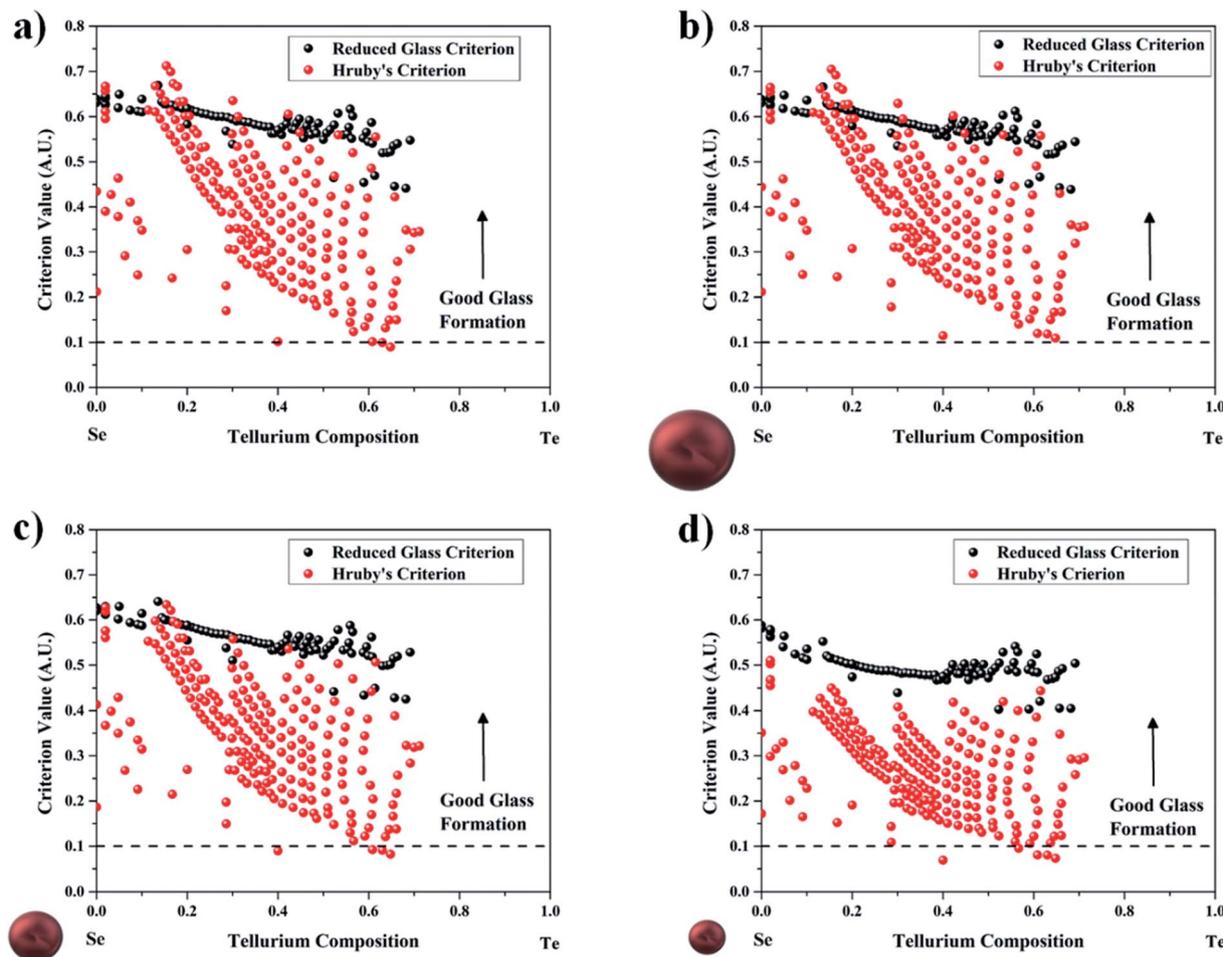
Fig. 9 Reduced glass criterion and Hruby's criterion for the (a) bulk, and spherical particle morphologies with sizes equal to (b) 50 nm, (c) 10 nm, and (d) 5 nm. Typically, those with a value greater than 0.1 in the Hruby's criterion are good glass formers.

reported for compositions greater than 80%, due to not high enough cooling rates when transitioning from the liquid to the glassy state.[24] For the crystalline phase, the material is reported to exist across the entire composition as seen in ref. 72. Also in that reference, they reported the energy bandgap of the crystalline phase to exhibit some bowing. The energy bandgaps of the amorphous and crystalline phases are consequently given by:

$$E_{g,\infty}^{a\text{-SeTe}}(x) = 1.84 - 1.50x \tag{15a}$$

$$E_{g,\infty}^{c\text{-SeTe}}(x) = 0.35x + 1.73(1 - x) - 1.102x(1 - x) \tag{15b}$$

From this and with eqn (16a) and (16b), respectively, the refractive index and high-frequency dielectric constant are plotted in Fig. 10b and c, respectively. The refractive index (16a) and high-frequency dielectric constant (eqn (16b)) of $Se_{1-x}Te_x$ (ref. 73) are modelled using the following:

$$n^{Se\text{-}Te}(x) = k^{1/4}[E_g^{Se\text{-}Te}(x)]^{-1/4} \tag{16a}$$

$$\varepsilon_{\infty}^{Se\text{-}Te}(x) = [n^{Se\text{-}Te}(x)]^2 \tag{16b}$$

where $\varepsilon_{\infty}^{Se\text{-}Te}(x)$ and $n^{Se\text{-}Te}(x)$ are the high-frequency dielectric constant and refractive index of $Se_{1-x}Te_x$ at a composition x, respectively. k is a constant equal to 95 eV. By using eqn (16a) and (16b), the refractive index and high frequency dielectric constant of $Se_{1-x}Te_x$ can be determined as a function of the chemical composition of the alloy.

The exciton Bohr radius is a measure of when a material becomes quantum confined and is expressed as follows:[73]

$$a_{B,ex}^{Se\text{-}Te}(x) = \varepsilon_{\infty}^{Se\text{-}Te}(x)\frac{m_e}{\mu(x)}a_0 \tag{17}$$

where $\varepsilon_{\infty}^{Se\text{-}Te}(x)$ is the high-frequency dielectric constant of $Se_{1-x}Te_x$, m_e is the rest mass of an electron, 9.11×10^{-31} kg, a_0 is the atomic Bohr radius, 0.053 nm, and $\mu(x)$ is the exciton reduced mass given by $\frac{1}{\mu(x)} = \frac{1}{m_e^*(x)} + \frac{1}{m_h^*(x)}$ where $m_e^*(x)$ and $m_h^*(x)$ are the effective mass of the electron and hole, respectively.

The exciton Bohr radius of $Se_{1-x}Te_x$ can be calculated by using the relationship between the exciton Bohr radius and the energy bandgap established in ref. 73:

$$\log[a_{B,ex}^{Se\text{-}Te}(x)] = \xi + \eta \log[E_{g,\infty}^{Se\text{-}Te}(x)] \tag{18}$$

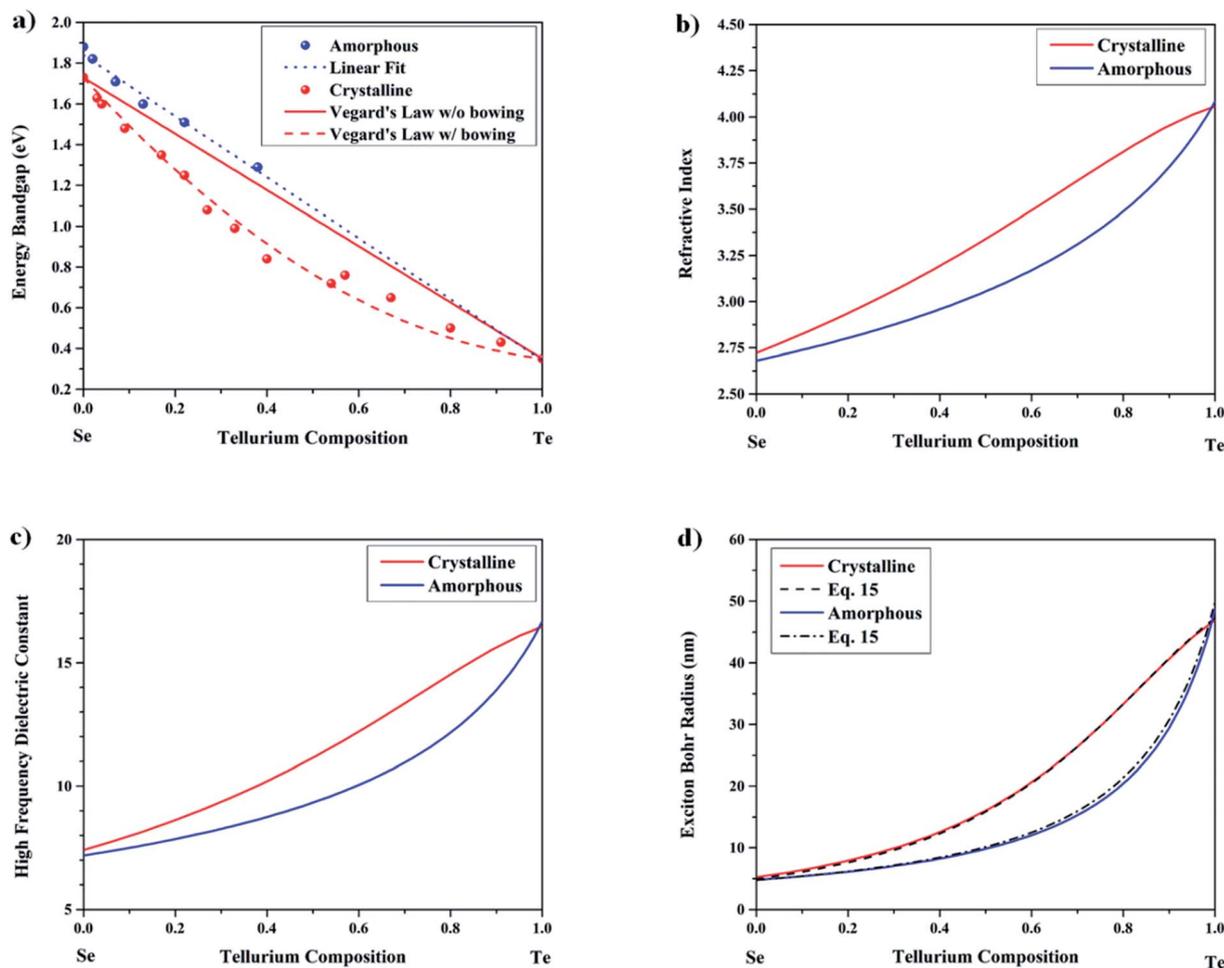**Fig. 10** (a) Energy bandgap *versus* the Te composition of the bulk $Se_{1-x}Te_x$ alloy. Experimental data points taken from ref. 21 for the amorphous case and ref. 72 for the crystalline case. (b) Refractive index *versus* the Te composition for the amorphous and crystalline cases. (c) High-frequency dielectric constant *versus* the Te composition for the amorphous and crystalline cases. (d) Exciton Bohr radius *versus* the Te composition calculated according to ref. 73 for the amorphous and crystalline cases, and curve fitting by eqn (17) using the calculated high-frequency dielectric constant from Fig. 8c and assuming a linear exciton effective mass for the amorphous case and Vegard's law like with bowing for the crystalline case.

where $a_{B,ex}^{Se-Te}(x)$ and $E_{g,\infty}^{Se-Te}(x)$ are the exciton Bohr radius and the bulk energy bandgap of $Se_{1-x}Te_x$ at a composition x, respectively. ξ and η are the fitting parameters given as 1.04434 ± 0.04976 and -1.37696 ± 0.10488, respectively.[73] Fig. 10d shows the amorphous and crystalline exciton Bohr radius as given by eqn (18). The exciton Bohr radius of a semiconductor material is of primary importance to determine the onset of quantum confinement effects. By using eqn (17) and (18), the material's exciton reduced mass, $\mu(x)$, was determined. In order to achieve this, the exciton reduced mass was assumed to vary linearly with the composition, which seems reasonable based on the data gathered from ref. 74. Indeed, Beyer *et al.* determined experimentally from conductivity measurements that the hole reduced mass varied linearly. Adopting this allows for good fitting found in comparison to eqn (17) (Fig. 9d). The exciton reduced masses for the amorphous and crystalline states are consequently described by:

$$\mu^{a-SeTe}(x) = 0.01775x + 0.08(1-x) \qquad (19a)$$

$$\mu^{c-SeTe}(x) = 0.0185x + 0.08(1-x) - 0.048x(1-x) \qquad (19b)$$

By increasing the Te composition, the reduced mass of $Se_{1-x}Te_x$ decreases. The exciton effective mass for the pure amorphous and the crystalline structures of Se is $0.080m_e$ while the exciton effective mass of crystalline Te is $0.019m_e$. According to Beyer *et al.*,[74] a fairly heavy hole effective mass, evolving as $m_h^*(x) = 1.4m_e(1-x) + 0.2m_ex$, is expected in $Se_{1-x}Te_x$ alloys. A large hole effective mass is common in some material systems such as Si and GaN,[73] where it is shown that it makes a very low contribution to the quantum confinement of those structures. This is very apparent by examining Te on its own which has a very large hole effective mass, $1.4m_e$. In contrast, Se has a much smaller hole effective mass, commonly found in semiconductor systems (*i.e.*, AlN, AlP, AlAs, InN, InP, InAs), consequently showing contributions from both the hole and the electron in the exciton effective mass. This suggests that there is a strong change in the band structure of this alloy. Further theoretical studies using DFT and experiments using Angle

Resolved Photo-Electron Spectroscopy (ARPES) should be performed to provide a better insight into the band structure of Se, Te, and $Se_{1-x}Te_x$. These studies are out of the scope of this paper.

In order to determine the energy bandgap of $Se_{1-x}Te_x$ at the nanoscale, the following scaling law is used:[36]

$$\frac{E_g^{Se-Te}}{E_{g,\infty}^{Se-Te}} = 1 + \left(\frac{\alpha_{shape}(x)}{D}\right) \tag{20}$$

where $E_{g,\infty}^{Se-Te}$ and E_g^{Se-Te} are the bulk and size-dependent energy bandgaps of $Se_{1-x}Te_x$ at a fixed composition, x. In the case of an alloy, $\alpha_{shape}(x)$ becomes composition-dependent. Eqn (20) is valid for sizes larger than the exciton Bohr radius of the material.[36]

By using eqn (20), the energy bandgap of $Se_{1-x}Te_x$ as a function of its chemical composition and size can be calculated and it is illustrated in Fig. 11 for the sphere, wire, and film morphologies. The region where the size is below the
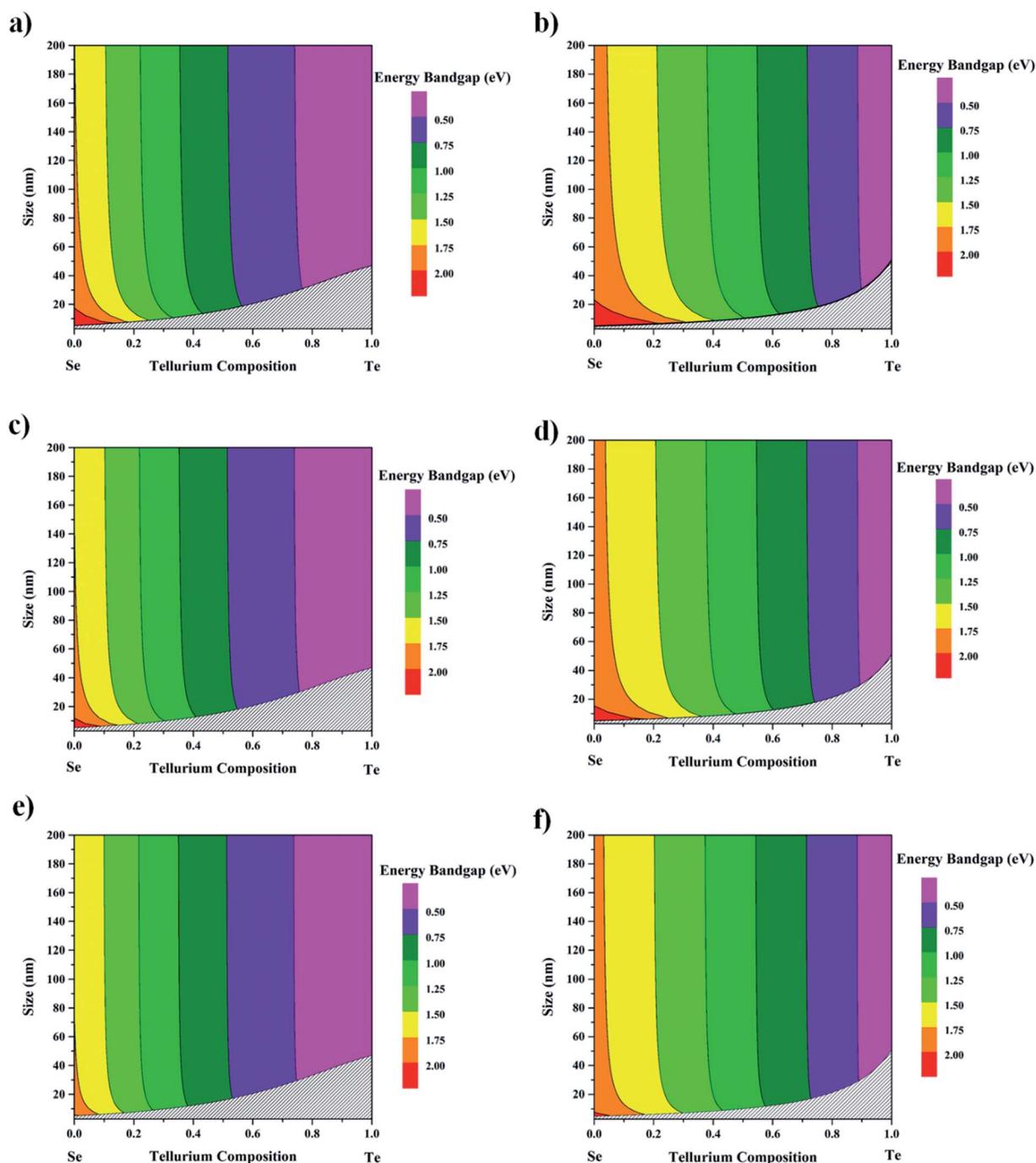

Fig. 11 Contour plots displaying the energy bandgap of the $Se_{1-x}Te_x$ alloy *versus* the Te composition and size of the alloy in crystalline and amorphous states for the (a and b) sphere, (c and d) wire, and (e and f) film morphologies. Areas in grey are the respective exciton Bohr radii for the crystalline and amorphous phases.
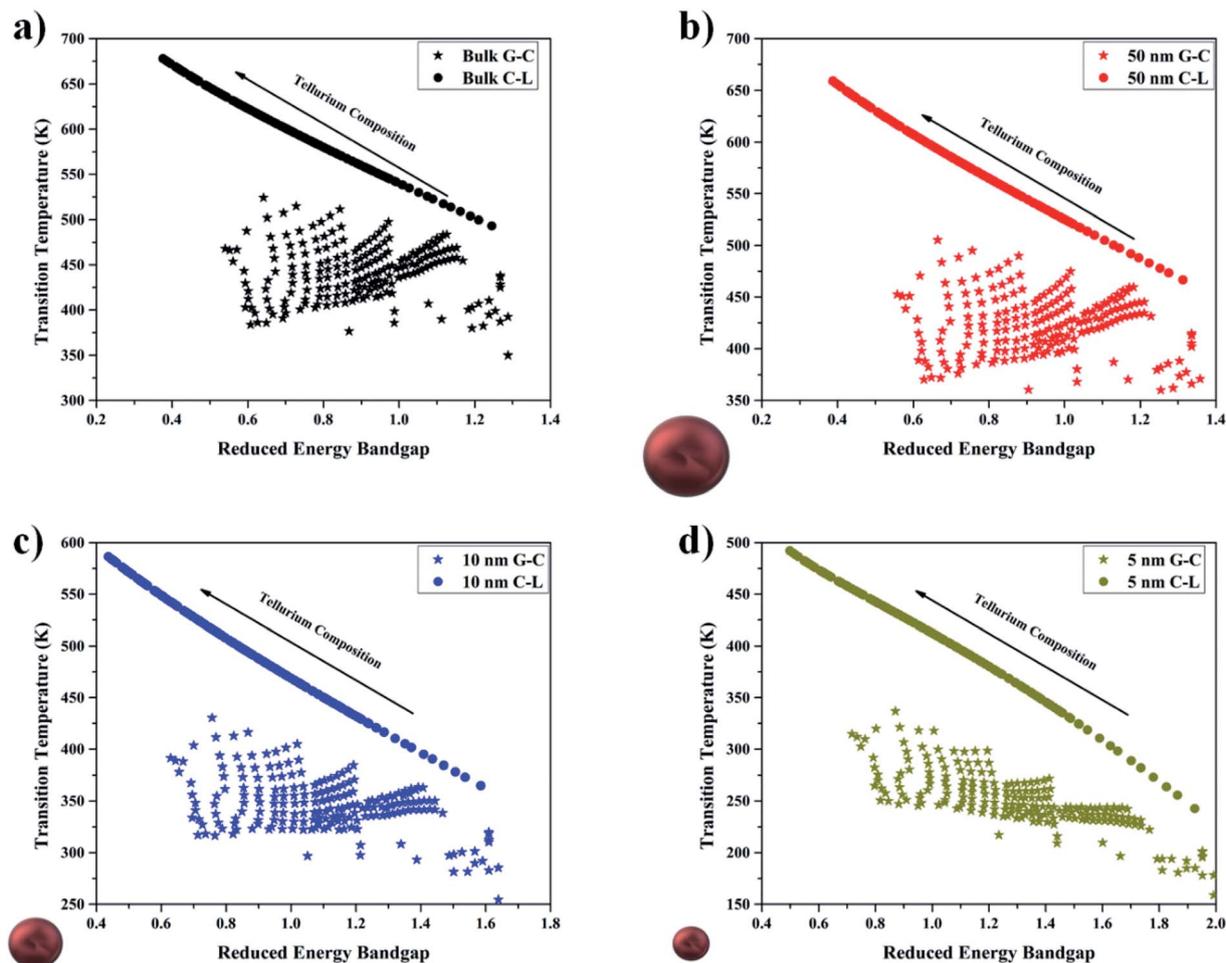
Fig. 12   Transition temperature *vs.* reduced energy bandgap of the amorphous (stars) and crystalline (circles) phases for the (a) bulk and nano-sized spherical nanoparticles with sizes equal to (b) 50 nm, (c) 10 nm, and (d) 5 nm.

exciton Bohr radius, is indicated in grey in Fig. 11. The sphere displays the largest size effect compared to the wire and the film because $\alpha_{sphere} > \alpha_{wire} > \alpha_{film}$; see Table 2. In order to use those nanostructures in solar cells, it has been demonstrated by Zdanowicz *et al.*[75] that the best energy bandgap to absorb the solar light was ~1.39 eV for a cell having only one single absorbing material. Therefore, the green areas in Fig. 11 are the most adequate regions to select the nanostructures from. This region corresponds to a chemical composition of Te varying between 20 and 40%. Above ~2 eV, the region in red in Fig. 11 represents the nanostructures that could be used in wide-bandgap semiconductor applications such as biological and chemical sensors.[76] Special consideration should be given to the crystallinity (crystalline or amorphous) and morphology (sphere, wire, and film) when selecting materials for this purpose. From Fig. 11, it is clear that nanoparticles are best for wide-bandgap semiconductor applications by comparison to wires or films. Indeed, wires and films only appear to be the right material properties to cater to these applications at very small sizes, *i.e.*, below 20 nm, and below 20% Te composition.

8.   Material selection for solar cell technology

Fig. 12a–d show the transition temperature *versus* the reduced bandgap energy of $Se_{1-x}Te_x$ alloys at various sizes (bulk, 50 nm, 10 nm, and 5 nm). The reduced bandgap energy is defined as the observed energy bandgap divided by the target bandgap, which results in the optimal value being 1. For a glassy material, the crystalline temperature is used as the transition temperature since a material should remain in the glassy state unless the temperature is above the crystalline transition temperature. For crystalline materials, the *liquidus* temperature is used as the transition temperature. This kind of plot elucidates which materials and under which conditions it might be appropriate to use bulk or nanoparticle morphologies for solar cell technologies. As stated previously, an energy bandgap around 1.39 eV has been shown to be the optimal bandgap for a material to harvest solar energy. Due to this, a large number of Te-rich alloys would not be advantageous to use for these goals as they predominantly have bandgaps bellow 1.39. However, this may not be a hard and fast rule for material selection as

shown in ref. 10 wherein by using a broad range of sizes of Te nanoparticles they were able to absorb 85% of the solar spectrum. Another condition that is necessary to impose is that of the transition temperature; if a material undergoes a phase change then the material properties change which results in the material becoming something else. For example, for a bulk $Se_{0.6}Te_{0.4}$ material, the bandgap energy of the crystalline state is 0.84 eV, while the amorphous phase has a bandgap of 1.23 eV, which results in a difference of ~0.4 eV. This kind of transition does not bode well for any material system that relies on a specific material property. Solar cells typically operate between 20 °C and 50 °C, so a material should not experience a transition in this window. This condition limits our search to particles with sizes above 10 nm and with compositions around 0.3.

9. Conclusions

In conclusion, the thermal and optoelectronic properties of $Se_{1-x}Te_x$ alloys are investigated and discussed. It is found that the properties are strongly size-dependent, *i.e.*, both Se and Te have large α_{shape} parameters. Se naturally segregates preferentially at the surface of the alloy at the nanoscale. The surface segregation energy has been determined at the bulk scale to be equal to −16.8 kJ mol^{-1}. Debye and Einstein temperatures of Se, Te, and $Se_{1-x}Te_x$ were investigated and were found to be in good agreement with the model proposed here in. Additionally, a logistic regression model was introduced to determine where the boundary between amorphous and crystalline states is. This model was extended to the nanoscale through nano-thermodynamics. The exciton Bohr radius of $Se_{1-x}Te_x$ increases with the Te composition. $Se_{1-x}Te_x$ nanostructures with a Te composition ranging between 20 and 40% are the most adequate structures to be used in solar cells.

Data availability

The data that support the findings of this study are available within the article and from the corresponding author upon reasonable request.

Conflicts of interest

There are no conflicts to declare.

References

1 A. J. Hurd, *et al.*, Energy-critical elements for sustainable development, *MRS Bull.*, 2012, **37**, 405–410.

2 R. Jaffe, *et al.*, *Energy Critical Elements: Securing Materials for Emerging Technologies*, POPA Reports, February 2011, pp. 1–28.

3 https://www.rsc.org/periodic-table/element/34/selenium.

4 https://www.rsc.org/periodic-table/element/52/tellurium.

5 J. E. Hoffmann, Recovering Selenium and Tellurium from Copper Refinery Slimes, *JOM*, 1989, 33–38.

6 W. K. Metzger, *et al.*, Recombination kinetics and stability in polycrystalline Cu(In,Ga)Se-2 solar cells, *Thin Solid Films*, 2009, **517**, 2360–2364.

7 X. Z. Wu, High-efficiency polycrystalline CdTe thin-film solar cells, *Sol. Energy*, 2004, **77**, 803–814.

8 T. A. M. Fiducia, *et al.*, Understanding the role of selenium in defect passivation for highly efficient selenium-alloyed cadmium telluride solar cells, *Nat. Energy*, 2019, **4**, 504–511.

9 W. Martienssen and H. Warlimont, *Springer Handbook of Condensed Matter and Materials Data*, Springer Berlin Heidelberg, Germany, 2005.

10 C. Ma, *et al.*, The optical duality of tellurium nanoparticles for broadband solar energy harvesting and efficient photothermal conversion, *Sci. Adv.*, 2018, **4**, eaas9894.

11 A. Eftekhari, The rise of lithium–selenium batteries, *Sustainable Energy Fuels*, 2017, **1**(1), 14–29.

12 G.-L. Xu, *et al.*, Selenium and Selenium–Sulfur Chemistry for Rechargeable Lithium Batteries: Interplay of Cathode Structures, Electrolytes, and Interfaces, *ACS Energy Lett.*, 2017, **2**(3), 605–614.

13 P. Dong, *et al.*, In situ surface protection of lithium metal anode in Lithium–Selenium disulfide batteries with ionic liquid-based electrolytes, *Nano Energy*, 2020, **69**, 104434.

14 R. Svoboda, M. Kincl and J. Málek, Thermal characterization of Se–Te thin films, *J. Alloys Compd.*, 2015, **644**, 40–46.

15 G. Guisbiers, *et al.*, Anti-bacterial selenium nanoparticles produced by UV/VIS/NIR pulsed nanosecond laser ablation in liquids, *Laser Phys. Lett.*, 2015, **12**(1), 016003.

16 G. Guisbiers, *et al.*, Inhibition of *E. coli* and *S. aureus* with selenium nanoparticles synthesized by pulsed laser ablation in deionized water, *Int. J. Nanomed.*, 2016, **11**, 3731–3736.

17 B. Hosnedlova, *et al.*, Nano-selenium and its nanomedicine applications: a critical review, *Int. J. Nanomed.*, 2018, **13**, 2107–2128.

18 H. H. Lara, *et al.*, Synergistic antifungal effect of chitosan-stabilized selenium nanoparticles synthesized by pulsed laser ablation in liquids against Candida albicans biofilms, *Int. J. Nanomed.*, 2018, **13**, 2697–2708.

19 H. W. Tan, *et al.*, Selenium Species: Current Status and Potentials in Cancer Prevention and Therapy, *Int. J. Mol. Sci.*, 2019, **20**(1), 75.

20 G. Guisbiers, *et al.*, Synthesis of tunable tellurium nanoparticles, *Semicond. Sci. Technol.*, 2017, **32**(4), 04lt01.

21 A. Mendoza-Galván, *et al.*, Structural, optical and electrical characterization of amorphous Se_xTe_{1-x} thin film alloys, *Microelectron. Eng.*, 2000, **51–52**, 677–687.

22 Z. H. Khan, *et al.*, Electrical and optical properties of a-Se_xTe_{100-x} thin films, *Opt. Laser Technol.*, 2012, **44**(1), 6–11.

23 K. Tripathi, *et al.*, Optical properties of selenium–tellurium nanostructured thin film grown by thermal evaporation, *Phys. B*, 2009, **404**(16), 2134–2137.

24 P. A. Vermeulen, J. Momand and B. J. Kooi, Reversible amorphous-crystalline phase changes in a wide range of $Se_{1-x}Te_x$ alloys studied using ultrafast differential scanning calorimetry, *J. Chem. Phys.*, 2014, **141**, 024502.

25 S. Fu, et al., One-step synthesis of high-quality homogenous Te/Se alloy nanorods with various morphologies, CrystEngComm, 2015, 17(17), 3243–3250.

26 H. Tao, et al., Solution Grown Se/Te Nanowires: Nucleation, Evolution, and The Role of Trigonal Te seeds, Nanoscale Res. Lett., 2009, 4(9), 963–970.

27 N. Metropolis and S. Ulam, The Monte Carlo Method, J. Am. Stat. Assoc., 1949, 44, 335–341.

28 H. Zhang, et al., Molecular Dynamics Simulations, Thermodynamic Analysis, and Experimental Study of Phase Stability of Zinc Sulfide Nanoparticles, J. Phys. Chem. B, 2003, 107(47), 13051–13060.

29 T. L. Hill, Thermodynamics of Small Systems, J. Chem. Phys., 1962, 36(12), 3182–3197.

30 T. Li and G. Galli, Electronic Properties of MoS_2 Nanoparticles, J. Phys. Chem. C, 2007, 111(44), 16192–16196.

31 J. Carrasquilla, Machine learning for quantum matter, Adv. Phys.: X, 2020, 5, 1797528.

32 O. V. Prezhdo, Advancing Physical Chemistry with Machine Learning, J. Phys. Chem. Lett., 2020, 11, 9656–9658.

33 G. Kaptay, Nano-Calphad: extension of the Calphad method to systems with nano-phases and complexions, J. Mater. Sci., 2012, 47(24), 8320–8335.

34 G. Kaptay, Thermodynamic Stability of Nano-grained Alloys Against Grain Coarsening and Precipitation of Macroscopic Phases, Metall. Mater. Trans. A, 2019, 50, 4931–4947.

35 A. Vegh and G. Kaptay, Modelling surface melting of macro-crystals and melting of nano-crystals for the case of perfectly wetting liquids in one-component systems using lead as an example, Calphad, 2018, 63, 37–50.

36 G. Guisbiers, Advances in thermodynamic modelling of nanoparticles, Adv. Phys.: X, 2019, 4(1), 1668299.

37 D. Bedeaux and S. Kjelstrup, Hill's nano-thermodynamics is equivalent with Gibbs' thermodynamics for surfaces of constant curvatures, Chem. Phys. Lett., 2018, 707, 40–43.

38 R. V. Chamberlin, The Big World of Nanothermodynamics, Entropy, 2015, 17, 52–73.

39 T. L. Hill, A different approach to nanothermodynamics, Nano Lett., 2001, 1(5), 273–275.

40 http://www.nasonline.org/publications/biographical-memoirs/memoir-pdfs/hill-terrell.pdf.

41 W. Qi, Nanoscopic Thermodynamics, Acc. Chem. Res., 2016, 49, 1587–1595.

42 W. Hume-Rothery, W. M. Gilbert and K. M. C. Evans, The freezing points, melting points, and solid solubility limits of the alloys of sliver and copper with the elements of the b sub-groups, Philos. Trans. R. Soc., A, 1997, 233(721–730), 1–97.

43 G. Ghosh, et al., The Se–Te (Selenium–Tellurium) system, J. Phase Equilib., 2007, 15(2), 213–224.

44 M. F. Kotkata, E. A. Mahmoud and M. K. El-Mously, Equilibrium diagram of Selenium—Tellurium system, Acta Phys. Acad. Sci. Hung., 1981, 50(1), 61–66.

45 G. Guisbiers, Size-Dependent Materials Properties Toward a Universal Equation, Nanoscale Res. Lett., 2010, 5(7), 1132–1136.

46 K. K. Nanda, Size-dependent melting of nanoparticles: Hundred years of thermodynamic model, Pramana, 2009, 72, 617–628.

47 D. M. Foster, et al., Atomic-resolution imaging of surface and core melting in individual size-selected Au nanoclusters on carbon, Nat. Commun., 2019, 10, 2583.

48 S. Inasawa, M. Sugiyama and Y. Yamaguchi, Laser-induced shape transformation of gold nanoparticles below the melting point: the effect of surface melting, J. Phys. Chem. B, 2005, 109(8), 3104–3111.

49 U. Tartaglino, et al., Melting and nonmelting of solid surfaces and nanosystems, Phys. Rep., 2005, 411, 291–321.

50 F. L. Williams and D. Nason, Binary alloy surface compositions from bulk alloy thermodynamic data, Surf. Sci., 1974, 45(2), 377–408.

51 D. Tománek, et al., Calculation of chemisorption and absorption induced surface segregation, Surf. Sci., 1982, 114(1), 11–22.

52 R. Mendoza-Perez and G. Guisbiers, Bimetallic Pt–Pd nano-catalyst: size, shape and composition matter, Nanotechnology, 2019, 30, 305702.

53 L. D. Geoffrion and G. Guisbiers, Chemical Ordering in $Bi_{1-x}Sb_x$ Nanostructures: Alloy, Janus or Core-Shell?, J. Phys. Chem. C, 2020, 124(25), 14061–14068.

54 G. Guisbiers, et al., Electrum, the Gold-Silver Alloy, from the Bulk Scale to the Nanoscale: Synthesis, Properties, and Segregation Rules, ACS Nano, 2016, 10(1), 188–198.

55 Q. Jiang and Z. Wen, Thermodynamics of Materials, Springer, 2011.

56 J. G. Dash, History of the search for continuous melting, Rev. Mod. Phys., 1999, 71(5), 1737–1743.

57 M. M. Vopson, N. Rogers and I. Hepburn, The generalized Lindemann melting coefficient, Solid State Commun., 2020, 318, 113977.

58 H. Ikemoto, et al., The size dependence of the Einstein temperature of the tellurium nanoparticles, J. Phys.: Conf. Ser., 2009, 190, 012126.

59 Y. H. Zhao and K. Lu, Grain-size dependence of thermal properties of nanocrystalline elemental selenium studied by X-ray diffraction, Phys. Rev. B: Condens. Matter Mater. Phys., 1997, 56(22), 14330–14337.

60 S. A. Kozyukhin, Anomalous mechanical properties of tellurium-modified glassy selenium, Inorg. Mater., 2006, 42(2), 210–214.

61 G. Carini, et al., Elastic constants of $Se_{1-x}Te_x$ solid amorphous alloys — the role of tellurium, J. Non-Cryst. Solids, 1984, 64(3), 317–324.

62 Y. Liu, et al., Materials discovery and design using machine learning, J. Materiomics, 2017, 3, 159–177.

63 F. Pedregosa, et al., Scikit-learn: Machine Learning in Python, J. Mach. Learn. Res., 2011, 12, 2825–2830.

64 G. Guo, et al., KNN Model-Based Approach in Classification, Springer Berlin Heidelberg, Berlin, Heidelberg, 2003.

65 A. S. Ahmad, et al., A review on applications of ANN and SVM for building electrical energy consumption forecasting, Renewable Sustainable Energy Rev., 2014, 33, 102–109.

66 G. Guisbiers, *et al.*, Inhibition of Candida albicans biofilm by pure selenium nanoparticles synthesized by pulsed laser ablation in liquids, *Nanomedicine*, 2017, **13**, 1095–1103.

67 D. Turnbull, Under what conditions can a glass be formed?, *Contemp. Phys.*, 1969, **10**, 473–488.

68 C. Suryanarayana, I. Seki and A. Inoue, A critical analysis of the glass-forming ability of alloys, *J. Non-Cryst. Solids*, 2009, **355**, 355–360.

69 M. L. F. Nascimento, *et al.*, Can glass stability parameters infer glass forming ability?, *J. Non-Cryst. Solids*, 2005, **351**, 3296–3308.

70 M. Saad and M. Poulain, Glass forming ability criterion, *Mater. Sci. Forum*, 1987, **19–20**, 11–18.

71 A. R. Denton and N. W. Ashcroft, Vegard's law, *Phys. Rev. A: At., Mol., Opt. Phys.*, 1991, **43**, 3161.

72 I. Hadar, *et al.*, Nonlinear Band Gap Tunability in Selenium–Tellurium Alloys and Its Utilization in Solar Cells, *ACS Energy Lett.*, 2019, **4**, 2137–2143.

73 L. D. Geoffrion and G. Guisbiers, Quantum confinement: size on the grill!, *J. Phys. Chem. Solids*, 2020, **140**, 109320.

74 W. Beyer, H. Mell and J. Stuke, Conductivity and thermoelectric power of trigonal Se_xTe_{1-x} single crystals, *Phys. Status Solidi B*, 1971, **45**, 153–162.

75 T. Zdanowicz, T. Rodziewicz and M. Zabkowska-Waclawek, Theoretical analysis of the optimum energy band gap of semiconductors for fabrication of solar cells for applications in higher latitudes locations, *Sol. Energy Mater. Sol. Cells*, 2005, **87**, 757–769.

76 S. J. Pearton, *et al.*, Recent advances in wide bandgap semiconductor biological and gas sensors, *Prog. Mater. Sci.*, 2010, **55**, 1–59.

77 G. Guisbiers, S. Arscott and R. Snyders, An accurate determination of the surface energy of solid selenium, *Appl. Phys. Lett.*, 2012, **101**(23), 231606.

78 D. A. Olsen, R. W. Moravec and A. J. Osteraas, Critical surface tension values of Group VIA elements, *J. Phys. Chem.*, 1967, **71**(13), 4464–4466.

79 C. Y. Ho, R. W. Powell and P. E. liley, Thermal Conductivity of the Elements: A Comprehensive Review, *J. Phys. Chem. Ref. Data*, 1974, **3**, I-1–I-796.

80 https://www.usgs.gov/centers/nmic/selenium-and-tellurium-statistics-and-information.

81 W. Gierlotka and W.-H. Wu, The reoptimization of the binary Se–Te system, *Int. J. Mater. Res.*, 2012, **103**(6), 698–701.

82 A. Rohatgi, *WebPlotDigitizer*, 2017.